

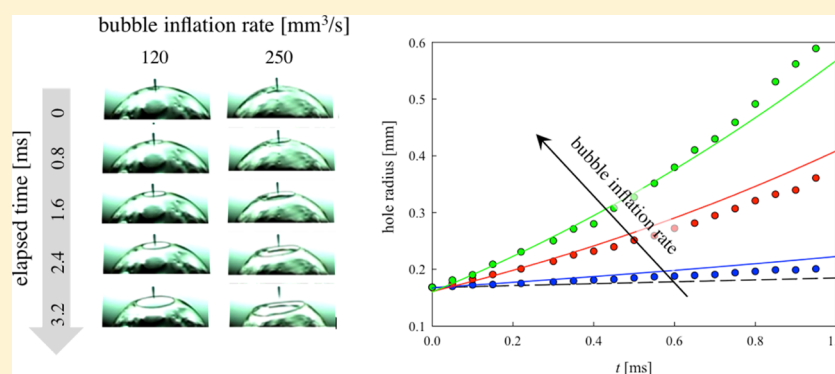
## Elasticity in Bubble Rupture

Daniele Tammaro,<sup>†</sup> Rossana Pasquino,<sup>†</sup> Massimiliano Maria Villone,<sup>\*,†</sup> Gaetano D'Avino,<sup>†,‡</sup> Vincenzo Ferraro,<sup>†</sup> Ernesto Di Maio,<sup>\*,†,‡</sup> Antonio Langella,<sup>†</sup> Nino Grizzuti,<sup>†</sup> and Pier Luca Maffettone<sup>†,‡</sup>

<sup>†</sup>Department of Chemical, Materials, and Manufacturing Engineering, University of Napoli Federico II, P.le Tecchio 80, 80125 Napoli, Italy

<sup>‡</sup>Institute of Applied Science and Intelligent Systems, National Research Council of Italy, Via Campi Flegrei 34, 80078 Pozzuoli, Naples, Italy

### Supporting Information



**ABSTRACT:** When a Newtonian bubble ruptures, the film retraction dynamics is controlled by the interplay of surface, inertial, and viscous forces. In case a viscoelastic liquid is considered, the scenario is enriched by the appearance of a new significant contribution, namely, the elastic force. In this paper, we investigate experimentally the retraction of viscoelastic bubbles inflated at different blowing rates, showing that the amount of elastic energy stored by the liquid film enclosing the bubble depends on the inflation history and in turn affects the velocity of film retraction when the bubble is punctured. Several viscoelastic liquids are considered. We also perform direct numerical simulations to support the experimental findings. Finally, we develop a simple heuristic model able to interpret the physical mechanism underlying the process.

## INTRODUCTION

Bubble rupture is of interest in a wide range of scientific and technological fields, for example, magma bubbling, aerosol formation, and oil and food industries. The very first observations of such a phenomenon were made in 1867 by Dupré,<sup>1</sup> who studied soap bubble rupture and modeled the retraction velocity of the hole rim through a balance between kinetic and surface energies. Almost a century later, Taylor<sup>2</sup> and Culick<sup>3</sup> independently derived the following mathematical expression for such velocity in the case of an inviscid liquid film

$$v_i = \sqrt{\frac{2\gamma}{\rho\delta}} \quad (1)$$

where  $\gamma$  is the surface tension between the liquid and the surrounding gas,  $\rho$  is the fluid density, and  $\delta$  is the film thickness. It readily follows from eq 1 that the hole radius increases linearly in time. At the opposite extreme, Debrégeas et al.<sup>4</sup> investigated the effect of fluid viscosity in the case of negligible inertia and derived an exponential growth law for the hole radius  $R$  that reads

$$R = R_0 \exp\left(\frac{\gamma t}{\eta\delta}\right) \quad (2)$$

where  $R_0$  is the initial hole radius,  $t$  is the time, and  $\eta$  is the fluid viscosity. The corresponding initial velocity of the retracting film  $v_0$  is then

$$v_0 = \frac{R_0\gamma}{\eta\delta} \quad (3)$$

In case a viscoelastic liquid is considered, the authors theorized an instantaneous elastic response against surface tension arising at hole formation.

The importance of liquid elasticity is well-documented in the breakup of cylindrical filaments (see ref 5 and the references therein). Such a phenomenon is relevant in all technological applications where a liquid goes through a nozzle, for example, ink-jet printing.<sup>6</sup> Specifically, fluid elasticity affects the necking and pinching of cylindrical threads, the breakup time, and the

**Received:** February 16, 2018

**Revised:** April 13, 2018

**Published:** April 17, 2018

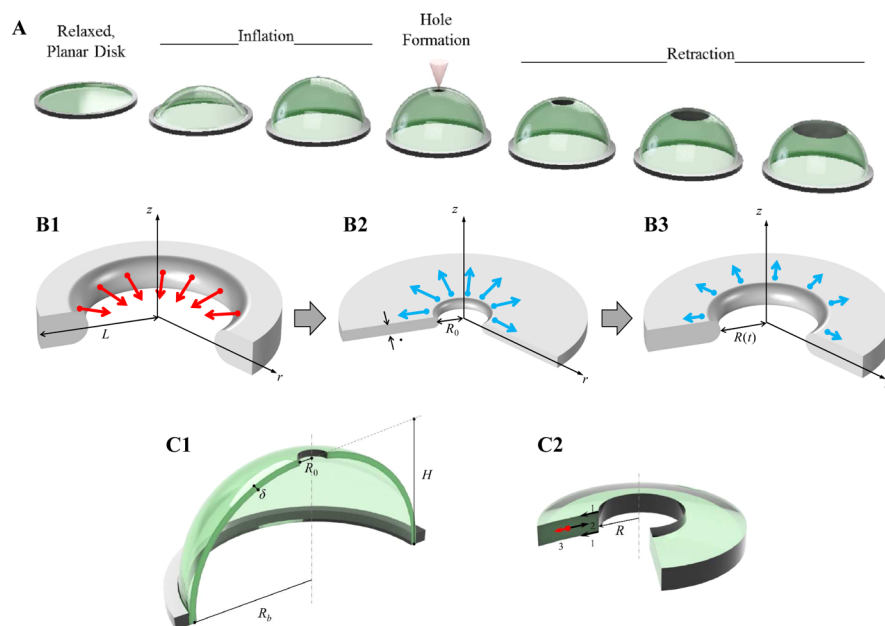


**Figure 1.** (A) Sketch of the experimental sequence including bubble inflation, hole formation, and film retraction. (B1) Sketch of the initial configuration of the numerical “equivalent” system, with the red arrows representing the applied stretching force. (B2) Sketch of the configuration of the numerical “equivalent” system at the end of the stretching phase, when the film is left free to retract. The cyan arrows qualitatively represent the retraction “driving force” felt by the film at this instant. (B3) Sketch of the configuration of the numerical “equivalent” system at a generic time during retraction, with the cyan arrows representing the residual net force acting on the film. (C1) Section of the geometry of the experimental system at hole formation, corresponding to the fourth image in panel A. (C2) Zoom of the film portion around the opening hole. Arrows denoted by 1, 2, and 3 indicate the surface, viscous, and elastic forces, respectively.

morphology of the “broken” portions of the filament (see, e.g., the papers by Cooper-White and co-workers<sup>7–9</sup>). Evers et al.<sup>10</sup> observed that the retraction velocity of flat thin viscoelastic films initially at rest is drastically slower than that of Newtonian films because of the intrinsic elasticity of the films.

For what concerns bubbles, the first experiments showing the effect of liquid elasticity were carried out very recently by Sabadini et al.<sup>11</sup> for very low-viscosity fluids and evidenced an unusual behavior in the rupture of viscoelastic bubbles, with a hole-opening velocity up to 30 times higher than the Taylor–Culick limit. The observed increase was attributed to an extra force related to the fluid elasticity working like an “equivalent elastic surface tension”. The authors mentioned the important role of elasticity relaxation for elastic bubble retraction, demonstrating that it was negligible in their experimental cases. They also put forth different physical scenarios to explain the bursting of a low-viscosity and high-elasticity bubble, however, without conclusive experimental evidence for proposing a unique model. Indeed, to correctly interpret the role of elasticity, the entire process of bubble inflation followed by bubble rupture needs to be taken into account, as the whole deformation history prior to bubble breakage is a fundamental ingredient. The common experience of bubble gum blowing gives intuitive evidence of the phenomenon: when gum inflation is slow, a hole produced with a needle does not broaden in time (see Figure S1A and the first part of Movie S1 online); conversely, if the inflation is fast, bubble burst is observed after hole formation (see Figure S1B and the second part of Movie S1). Hence, even in a very uncontrolled situation, film retraction appears to depend not only on the intrinsic fluid properties and bubble geometry but also on how the bubble approaches the rupture event.

To understand and quantify the effect of the deformation history on the retraction of viscoelastic bubbles, we carried out

a wide experimental campaign at varying bubble inflation rates and the liquid constituting the film. For one of the liquids investigated experimentally, direct numerical simulations (DNS) were also performed to enhance the comprehension of the initial opening dynamics in the proximity of the hole. Finally, a simple heuristic model aiming at interpreting the physical mechanism underlying the process was developed.

## RESULTS AND DISCUSSION

The significant technical challenge of setting up an experimental system able to control and measure the inflation rate (IR) of a bubble and to visualize its rupture and retraction was in order. A thin disc of a viscoelastic fluid was spread on a metallic ring with radius  $R_b$ ; then, it was blown by pumping air from below, as schematically depicted in the first three images in Figure 1A. Such a blowing protocol is similar to the one adopted to study bread dough extensional rheology (see, e.g., refs 12–16). The blowing phase ended when the bubble touched a needle making a hole on its top (fourth image in Figure 1A). The consequent hole-opening dynamics was recorded with a high-speed camera. Figure 1A reports a scheme of the experimental sequence including bubble inflation, hole formation, and film retraction.

Let us consider a 0.05 wt % solution of polyacrylamide in maple syrup with high constant viscosity and high relaxation time, referred to as the “PA1” in the following. Details on the fluid preparation are given in Materials, whereas its rheological characterization is explained in Fluid Characterization and reported in Figure S2, where it can be observed that the rheological properties of PA1 are typical of those of a class of materials known as “Boger fluids”.<sup>17</sup> A film made of such a liquid was inflated at three different (time-constant) IR-values, namely, 20, 120, and 250 mm<sup>3</sup>/s. In Figure 2A, two sequences

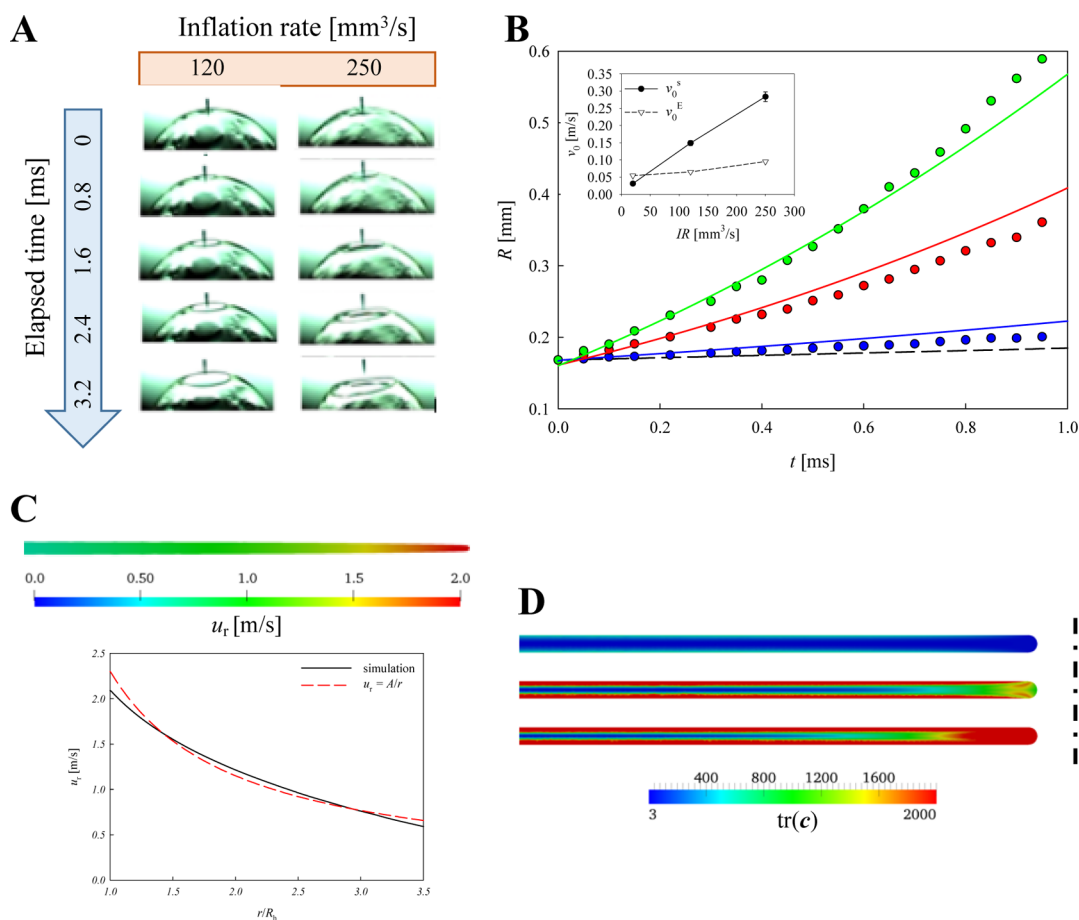


**Figure 2.** (A) Sequences of experimental images of the hole opening for PA1 at IR = 120 mm<sup>3</sup>/s (left) and IR = 250 mm<sup>3</sup>/s (right). (B) Comparison of the experimental (symbols) and DNS (solid lines) initial trends of the hole radius for PA1 at IR = 50 mm<sup>3</sup>/s (blue symbols and line), 120 mm<sup>3</sup>/s (red), and 250 mm<sup>3</sup>/s (green). The black dashed line reports the prediction for a viscous Newtonian film given by eq 2. The inset displays the initial values of the hole-opening velocity as a function of IR arising from experiments ( $v_0^s$ , full circles) and from eq 4 ( $v_0^e$ , empty triangles). The error bars are obtained by three measurements, and on the first two points, they are indistinguishable from the marker. (C) Color map of the radial component  $u_r$  of the liquid velocity in the film portion in proximity of the hole at  $t = 1.0$  ms and IR = 250 mm<sup>3</sup>/s and comparison between the numerical  $u_r$  profile and a fit through the model  $u_r = A/r$ . (D) Color maps of the trace of the conformation tensor  $\text{tr}(c)$  in the film cross section at the hole-opening initial instant arising from numerical simulations. Top, middle, and bottom images correspond to the low, medium, and fast stretching dynamics, respectively.

of high-speed images showing film retraction after inflation at the medium and high blowing rate are displayed. From the comparison of the snapshots taken at the same time instants, it is apparent that the hole broadens more quickly when IR is larger, *ceteris paribus*. It is also worth mentioning two features of the experimental images shown in Figure 2A. First, the bubble surface appears slightly “mottled”, possibly denoting a nonuniform thickness; however, the hole-opening velocity results, at varying inflation rates, are reproducible, as shown by the fact that the error bars (obtained by 3 measurements) on the experimental points reported in the inset in Figure 2B (discussed below) are in the order of 5%. Second, as the holes increase in radius, a rim forms around the hole perimeter. Rim formation is a well-known phenomenon concerning both Newtonian and non-Newtonian films, which arises due to the liquid inertial effects.<sup>18–22</sup> Thus, as rims form well beyond the initial stages of the hole-opening phenomenon ( $t > 1$  ms), they do not affect the dynamics of our interest.

The symbols in Figure 2B report the experimental values of the hole radius as a function of time for the three above mentioned values of the inflation rate. In all cases, the initial hole radius was 168  $\mu\text{m}$ . To emphasize the initial film retraction

dynamics, a time window going from hole formation ( $t = 0$ ) to 1 ms is shown. As also visible from Figure 2A, out of such a window, the system progressively lost its axial symmetry; thus, it is difficult to quantify the hole opening simply through radius measurements. The black dashed line in Figure 2B corresponds to the exponential hole radius growth for a viscous Newtonian film predicted by Debrégeas et al.<sup>4</sup> and given in eq 2. The data sets in Figure 2B clearly show that, even at the lowest inflation rate IR = 20 mm<sup>3</sup>/s, a viscoelastic bubble retracts faster than a Newtonian one. Furthermore, the hole-opening dynamics is progressively faster at increasing blowing rates. Such a feature can be ascribed to an increasing amount of elastic energy stored by the inflated film, all other parameters being the same. This result is in contrast with what reported by Evers et al.<sup>10</sup> in a situation with a very different initial condition. Indeed, in the case where the viscoelastic film is initially at rest, the effect of liquid elasticity is working against the surface tension, slowing down the film retraction with respect to a Newtonian liquid.

To support the experimental findings and deepen their physical interpretation, we performed finite element numerical simulations of a simplified system mimicking bubble inflation, puncturing, and film retraction process (see Direct Numerical

**Simulations**). A sketch of the numerical “equivalent” system is displayed in Figure 1B1–B3. We considered an annular disk of an inertialess Oldroyd-B viscoelastic liquid (see Mathematical Model in the Supporting Information) with the external cylindrical surface fixed in the radial direction and free to move in the axial direction (Figure 1B1). The constitutive parameters of the liquid were derived through a fit of the experimental rheological data shown in Figure S2 for PA1, as detailed in Mathematical Model. Different time-dependent displacement fields (schematically represented by the red arrows in Figure 1B1) were applied on the liquid domain boundaries, which made the film stretch in the direction of decreasing  $r$  until the central hole radius and the transversal film thickness reached the experimental values (see Figure 1B2). At this point, the external action was ceased; thus, the film was subjected to surface, viscous, and elastic forces, whose overall effect was a net force (the cyan arrows in Figure 1B2) making the hole open until reaching the final configuration dictated by the minimization of the film external surface. The geometrical parameters of the numerical “equivalent” system and the stretching laws were selected as to reproduce the experimental initial opening trends as much quantitatively as possible (see Supporting Information). The solid lines in Figure 2B report the numerical temporal trends of the hole radius for the three simulated stretching laws corresponding to the experimental IR values. It is apparent that in the time window shown in Figure 2B, a quantitative agreement holds between experimental and numerical data for all IR considered.

DNS can be a useful tool to extract information otherwise inaccessible from experiments. An interesting point is the velocity distribution in the film during retraction. In Figure 2C, we display the color map of the radial component  $u_r$  of the liquid velocity in the film portion in proximity of the hole at  $t = 1.0$  ms and  $IR = 250$  mm<sup>3</sup>/s. It is apparent that  $u_r$  is substantially constant in the sheet section along the axial direction and it decreases in the radial direction from the hole toward the wall. In Figure 2C, we also plot the radial  $u_r$  profile. As the model parameters and assumptions suggest, the retraction occurs in the viscous flow regime and we can compare the simulated velocity distribution (black solid line) with a fit through the model  $u_r = A/r$  (red dashed line). Such dependence is the one reported in ref 4 for a bare viscous bubble. The fit is qualitatively good, yet two main differences arise, that is, (i) the coefficient of the dashed red curve is 1 order of magnitude higher than the coefficient given in ref 4 for a Newtonian liquid with the same parameters as ours and (ii) the fit of the numerical data through the  $A/r$  model is not perfect. The first difference can be ascribed to the storage of elastic energy provided by the film, which speeds up its retraction, as discussed above (see also Figure 2B). The second is connected to elasticity: even if the retraction happens in the viscous flow regime, the film is not made of a purely viscous fluid. A very relevant aspect of our problem is the evaluation of the elastic energy stored by the liquid film as a result of inflation. Such a measurement can be provided by the trace of the conformation tensor<sup>23</sup> (see Mathematical Model). In Figure 2D, we show the color maps of this quantity in the film cross section right at the end of the stretching phase for the low (top), medium (middle), and high (bottom) stretching rates. It readily appears from the comparison among the three maps that the higher the stretching rate, the larger the amount of elastic energy stored by the liquid sheet, which in turn results

in a higher initial hole-opening velocity, as it appears from both experimental and numerical data in Figure 2B.

A simple description of the physics underlying the retraction mechanism can be attempted by considering the series of the two processes, that is, bubble inflation and hole opening, separated by the rupture event. On the one hand, viscoelastic liquids are able to elastically recover the stored deformation; on the other hand, they dissipate stress due to viscosity. The time scale on which stress is relaxed is given by the fluid relaxation time  $\tau_r$ . Hence, at a given relaxation time, a faster bubble inflation leads to a larger amount of elastic energy stored by the film, provided that the inflation time  $\tau_i$  is comparable with  $\tau_r$  (which is, indeed, the case of our experiments, where both  $\tau_i$  and  $\tau_r$  are of order unity as shown in the Supporting Information in Figure S6 and Table S1). It is worth mentioning that the inflation time  $\tau_i$  is linked to the inflation rate IR as  $\tau_i = V_b/IR$ , where  $V_b$  is the volume of the bubble at the end of inflation. The ratio  $\tau_r/\tau_i$  is the Deborah number for the inflation process  $De_i$ , giving a measure of the extent of the elastic energy buildup in such a process.<sup>24</sup> If no time is waited at the end of bubble blowing before puncturing the film (which would allow the liquid to further dissipate stress), increasing IR results in an increasing “long-time recoverable extensional deformation”  $\epsilon_E$ .<sup>25</sup> Such a quantity measures the amount of the film total elastic deformation that the liquid is able to recover and, together with the surface tension, it drives the film retraction. Note that, in general,  $\epsilon_E = \epsilon_E(IR, RT)$ , where RT is the resting time, always equal to 0 in our case.

Figure 1C1 displays a section of the geometry of the experimental system at hole formation. To model the initial dynamics of film retraction, let us consider the portion of the film surrounding the hole, shown in Figure 1C2. For the sake of simplicity, we assume that (i) the film thickness is uniform, (ii) the hole spreading is axisymmetric, (iii) the effects of gravity and curvature are negligible, that is, the portion of the film around the hole is almost flat (Figure 1C2), and (iv) the temperature is constant. Under these assumptions, a one-dimensional description of the hole opening suffices. At early stages, the film thickness can be considered constant, and the forces driving the hole dynamics are as follows: (i) the surface tension contribution  $F_\gamma = 4\pi R_0\gamma$ , (ii) the viscous contribution  $F_\eta = -4\pi\delta v_0^E\eta$ , and (iii) the elastic contribution  $F_E = 4\pi\delta R_0 E\epsilon_E$ , where  $v_0^E$  is the initial velocity of the retracting film<sup>4</sup> and  $E$  is the elastic modulus of the fluid (the other symbols having been defined above). Notice that because liquid viscosity acts against hole opening,  $F_\eta$  has the opposite sign with respect to  $F_\gamma$  and  $F_E$ , the latter both acting in favor of hole opening. Notice also that, in the expression of the viscous force  $F_\eta$  given above, it is assumed that the liquid has a constant viscosity; thus, the predictions yielded by the simple heuristic model developed in the following will be compared with the experimental data for the constant-viscosity PA1. We have intentionally kept inertia out of the picture as its contribution is negligible here because of the large viscosity of the fluid.<sup>26</sup> Indeed, for PA1, the inertial characteristic time can be estimated as  $\tau_p = \sqrt{\rho\delta^3/(2\gamma)} \approx 0.1$  ms which is far smaller than the other characteristic times at play. Likewise, the dimensionless parameter measuring the relevance of inertial effects, namely, the maximum Reynolds number  $Re_{\max} = \rho v_{0,\max}^E R_{\max}/\eta$ <sup>26</sup> is equal to about 0.008; thus, it can be considered sufficiently small to allow us to neglect inertia in our description. (To compute  $Re_{\max}$  we used the PA1 constitutive parameters given in Figure

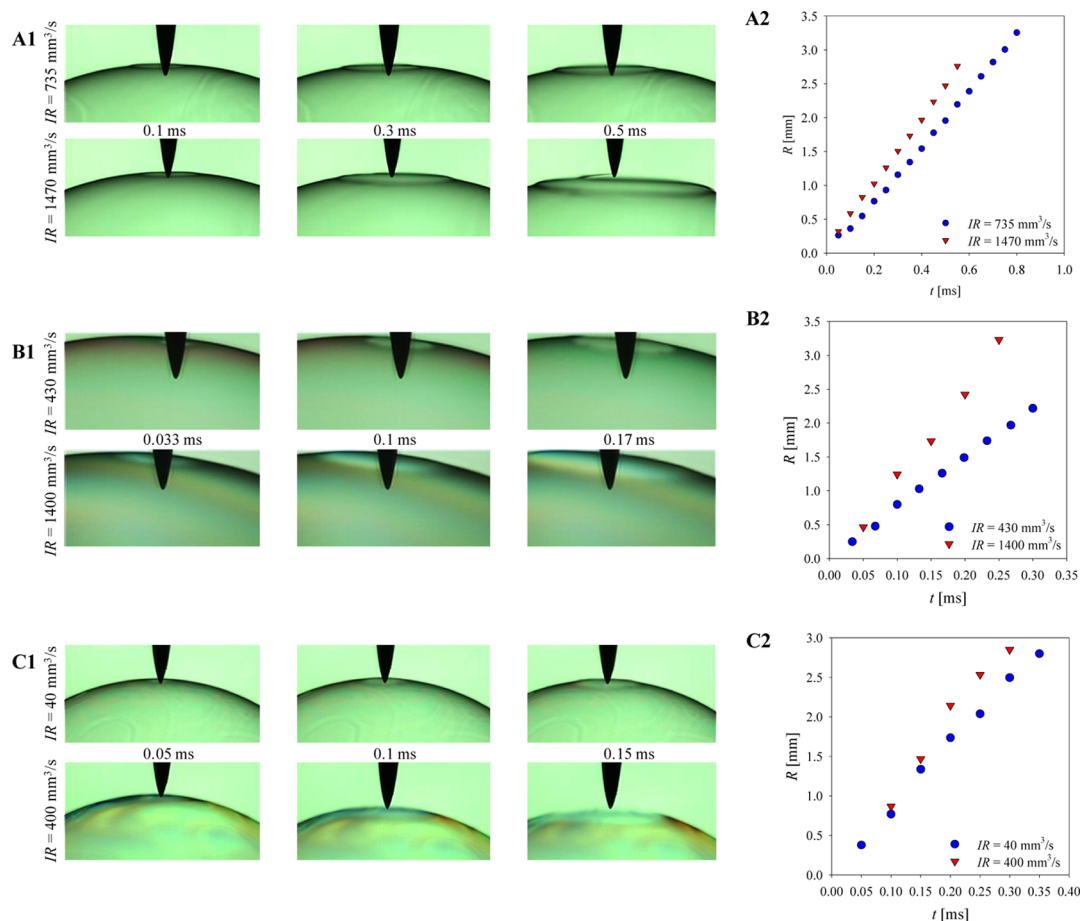


**Figure 3.** (A1) Sequences of experimental images of the hole opening for PA2 at two different IR values (see labels on the left). (A2) Experimental initial trends of the hole radius  $R(t)$  for PA2 at two different IR values (see legend). (B1) Sequences of experimental images of the hole opening for WMS1 at two different IR values (see labels on the left). (B2) Experimental initial trends of the hole radius  $R(t)$  for WMS1 at two different IR values (see legend). (C1) Sequences of experimental images of the hole opening for WMS2 at two different IR values (see labels on the left). (C2) Experimental initial trends of the hole radius  $R(t)$  for WMS2 at two different IR values (see legend).

S7 and Table S1 and the experimental data given in Figure 2B for the highest IR.) The initial hole-opening velocity  $v_0^E$  can be then determined by solving the force balance  $F_\gamma + F_\eta + F_E = 0$  and in dimensionless terms is

$$\frac{v_0^E}{v_0} = 1 + \frac{\delta}{R_0} E_C \varepsilon_E \quad (4)$$

where  $E_C = R_b E / \gamma$  is an elastocapillary number comparing elastic to surface forces.<sup>27</sup> In the left-hand side of eq 4,  $v_0^E$  is normalized by the initial retracting velocity for a viscous Newtonian film  $v_0$  (see eq 3). In the right-hand side (RHS) of eq 4, 1 is summed to a term embodying the viscoelastic contribution to film retraction, whose “ingredients”  $\delta/R_0$ ,  $E_C$ , and  $\varepsilon_E$  are intrinsically positive. Therefore, eq 4 gives the increase of the initial retracting velocity of a viscoelastic bubble, depending on the inflation rate, with respect to that of a viscous Newtonian film with the same parameters in the absence of inertia.

To compare the predictions of eq 4 with the experimental data, the values of  $\varepsilon_E$  corresponding to the experimental conditions were to be determined. During inflation, the liquid undergoes a deformation  $\varepsilon_i(t)$  imposed by the blowing apparatus, a part of which is not recoverable because of viscous dissipation. Figure S6 reports the experimental inflation

histories for PA1. The recoverable deformation  $\varepsilon_E$  can be computed from the integration of the following equation

$$2De_i \frac{d\varepsilon_D}{dt} = \varepsilon_i - \varepsilon_D, \quad \varepsilon_D(t=0) = 0 \quad (5)$$

where  $\varepsilon_D$  is the amount of deformation dissipated during the inflation process. The integration of eq 5 from 0 to  $\tau_i$  yields the long-time recoverable deformation at bubble breaking  $\varepsilon_E(\tau_i) = (\varepsilon_i - \varepsilon_D)|_{\tau_i}$ . For PA1, one obtains  $\varepsilon_E = 0.0033$ ,  $0.024$ , and  $0.079$  for the low, medium, and high inflation rate, respectively. When the inflation history is not exactly known or unavailable,  $\varepsilon_E$  can be estimated from the knowledge of the total applied deformation  $\varepsilon_T = \varepsilon_i(\tau_i)$  and the inflation time  $\tau_i$ . By assuming a step-strain deformation and a simple fading memory function,<sup>27</sup> the estimate can be performed as follows

$$\varepsilon_E \approx \varepsilon_T \exp\left(-\frac{\tau_i}{\tau_r}\right) = \varepsilon_T \exp\left(-\frac{1}{De_i}\right) \quad (6)$$

It is evident from eq 6 that, given the geometry of the inflated bubble and the fluid rheology, the faster the bubble is blown (i.e., the lower  $\tau_i$ ), the higher  $\varepsilon_E$  and thus the higher the initial hole-opening velocity  $v_0^E$ . The inset in Figure 2B shows the  $v_0^E$  values given by eq 4 as a function of IR and the corresponding experimental results for PA1. The values of the

rheological and geometrical parameters used to compute such results are reported in Table S1, yielding an elastocapillary number  $E_C = 2.84$ . The model is able to qualitatively reproduce the trend of the initial values of the hole-opening velocity at varying inflation rates. It is worth mentioning that because around the opening hole the liquid flow is close to a biaxial extensional flow, even if the model is one-dimensional, all rheological parameters appearing in eq 4 are estimated as six times the corresponding shear values.<sup>28</sup>

To assess the general validity of the findings on PA1 reported above, we performed a systematic experimental campaign on the breaking of bubbles made of three other viscoelastic liquids, namely, a 0.6 wt % polyacrylamide–0.34 wt % maple syrup aqueous solution (referred to as “PA2” in the following), a 100 mM cetylpyridinium chloride (CyPCL)–50 mM diclofenac wormlike micellar solution (referred to as “WMS1” in the following), and a 20 mM cetyltrimethylammonium bromide (CTAB)–20 mM sodium salicylate (NaSal) wormlike micellar solution (the same used by Sabadini et al. in ref 11, referred to as “WMS2” in the following). Further information on the composition and preparation protocol of such liquids is given in Materials, whereas their rheological characterization is reported in Figures S3–S5.

In Figure 3A1–C1, three pairs of sequences of high-speed images of the opening bubble are displayed, each pair referring to two different blowing rates of the same liquid film, that is, PA2 in Figure 3A1, WMS1 in Figure 3B1, and WMS2 in Figure 3C1. For each pair of sequences, as the snapshots are taken at the same time, it is apparent that the hole broadens faster when IR is larger. The symbols in Figure 3A2–C2 report the experimentally measured temporal trends of the hole radius for the three above mentioned fluids and for each at varying inflation rates. For each fluid, the time window is selected to show results as far as the film retraction can be quantified in terms of the hole radius. The data quantitatively confirm the effect of the bubble deformation history on its retraction dynamics.

It is worth mentioning that, at variance with the case of PA1 discussed above, for PA2, WMS1, and WMS2,  $R(t)$  is mostly linear in the observed time window (parametrically in the inflation rate). Such trends may suggest that for these three fluids, inertial effects also play a role. The estimation of the maximum Reynolds number  $Re_{\max}$  supports this idea. For example, with reference to WMS2, by using  $\rho \approx 1000 \text{ kg/m}^3$ ,  $\eta \approx 0.6 \text{ Pa s}$  (estimated from Figure S5A as six times the extrapolated value at the shear rate  $\sim 10^2 \text{ s}^{-1}$ ),  $v_{\max} \approx 10 \text{ m/s}$ , and  $R_{\max} \approx 3 \text{ mm}$  (estimated from Figure 3C2), we get  $Re_{\max} \approx 50$ , indicating that for this fluid, the film retraction is in the inertial regime.

From the rheological data of PA2, WMS1, and WMS2 reported in Figures S3–S5, it is apparent that at variance with the constant-viscosity PA1 (Figure S2), these liquids are shear thinning, namely, their viscosity decreases at increasing shear rates. Hence, for these fluids, a higher amount of stored elastic energy causes a higher initial hole-opening velocity, which, in turn, determines a viscosity decrease that further enhances the retraction velocity. Therefore, the observed behaviors are due to the synergy of effects that cannot be decoupled. However, it is worth remarking that the contribution of liquid elasticity is crucial for the occurrence of the observed phenomenon because a nonelastic shear-thinning liquid would not show any dependence of the retraction velocity on the inflation rate. Indeed, in such fluids, the hole-opening velocity only depends

on the geometry of the system and the surface tension between the liquid and the ambient fluid, which do not change within any of our experiments for each given liquid. In this regard, the results on PA1 shown in Figure 2A,B can be entirely ascribed to elastic energy storage and do not “suffer” from any effect due to shear thinning because PA1 has a viscosity that is independent of the flow intensity (see Figure S2A). Hence, this liquid is particularly well-suited for the purpose of our investigation.

In the light of the results discussed above, the role of viscoelasticity in natural and industrial processes involving bubble rupture can be now revisited in a more consistent and complete perspective. For example, in volcanic eruptions, the combination of magma viscoelastic properties and fast gas bubble inflation makes the additive term in the RHS of eq 4,  $E_C \epsilon_E$ , much larger than unity,<sup>29</sup> and thus, the retraction of magma films is explosive. At the opposite extreme, molten metals are very weakly elastic; therefore, almost no contribution from elasticity will arise during metal foaming.<sup>30</sup> Intermediate situations can be found in numerous fields: for example, in polymer foaming, the process kinetics can lead to closed- or open-cell structures, giving different acoustic and thermal insulating properties to the resulting materials.<sup>31</sup>

## CONCLUSIONS

In this paper, we investigated the retraction of viscoelastic bubbles. By experimentally testing numerous viscoelastic fluids, we showed that depending on the inflation rate, a different amount of elastic energy is stored by the liquid film enclosing the bubble, which in turn significantly influences the hole-opening velocity when the bubble is punctured. A quantitative support to the experimental results is provided by DNS. We also developed a simple heuristic model able to catch the physical mechanism underlying the process.

Identifying an explicit link between the inflation history and the retraction dynamics provides a tool to design new materials, as in the case of the different morphologies arising in polymeric foams,<sup>31,32</sup> to steer technologies involving bubbles, such as in oil or food industries,<sup>33,34</sup> and to understand natural phenomena, such as magma bubbling<sup>35,36</sup> and aerosol formation.<sup>26,37</sup>

## MATERIAL AND METHODS

**Materials.** Four viscoelastic fluids with different rheological properties have been selected to highlight the role of elasticity in bubble breaking. Two polymer-based and two surfactant-based solutions have been prepared. The first polymeric liquid is a 0.05 wt % solution of polyacrylamide (PA) (Saparan MG 500, The Dow Chemical Company) in maple syrup (Maple Joe, Famille Michaud Apiculture), whose preparation is reported in ref 17 (referred to as “PA1” in the text). The second polymer-based fluid is a 0.6 wt % polyacrylamide–0.34 wt % maple syrup aqueous solution (referred to as the “PA2” in the text).

A micellar solution based on the widely used surfactant CyPCL (AppliChem Panreac) has been prepared by using distilled water as a solvent and by adding the nonsteroidal anti-inflammatory drug diclofenac (Farmalabor) in its sodium form (referred to as “WMS1” in the text). The latter works as an aromatic cosolute, acting as a binding salt, creating long and interconnected wormlike micelles that confer elasticity to the surfactant solution. The surfactant concentration was 100 mM, whereas the diclofenac content was 50 mM. The solution has been prepared according to the protocol reported in refs 38 and 39. The other micellar solution is based on the work by Sabadini et al.<sup>11</sup> and is a 20 mM CTAB (Sigma-Aldrich) aqueous solution with 20 mM sodium salicylate (Sigma-Aldrich) as a binding salt (referred to as “WMS2” in the text). As in the case of WMS1, the

fluid is characterized by the presence of strongly interconnected very long wormlike micelles.

**Fluid Characterization.** The steady shear properties and the linear viscoelastic moduli of the liquids have been measured by means of a stress-controlled rheometer (Physica MCR702, Anton-Paar) with 25 mm parallel plates with a gap of 1 mm and 50 mm cone-plate geometry with an angle of  $1^\circ$ . The rheometer has been used in the single-motor mode at a temperature of  $25^\circ\text{C}$  controlled via a Peltier unit and an anti-evaporation block. A strain-controlled rheometer (Ares, TA Instruments) has been used for the sample PA1, with 50 mm cone-plate geometry and an angle of 0.02 rad. The choice of a smaller angle guarantees higher edge stability for the sample characterized by such high elasticity. In the case of PA1, the test has been performed at an ambient temperature, in controlled conditions. The heating equipment of the Ares is, indeed, a convection oven, which would have caused a faster evaporation of the sample. Steady shear measurements up to  $100\text{ s}^{-1}$  have been performed. Linear viscoelastic response has been studied in a range of angular frequency from 100 down to 0.1 rad/s to evaluate the relaxation time and the elastic modulus plateau of the liquids. The strain amplitude has been set large enough to give a reliable signal while keeping the measurements in the linear viscoelastic regime.

Figure S2 shows the rheological properties of PA1. As it is apparent from panel A, the viscosity of the liquid  $\eta$  is constant in the shear rate range and roughly equal to 3 Pa s; on the other hand, relevant values of the first normal stress difference  $N_1$  (almost quadratically dependent on  $\dot{\gamma}$ ) are measured. Such a behavior is typical of a class of materials known as “Boger fluids”. At high shear rate values, the viscosity response (coherently with literature<sup>40</sup>) shows elastic instability. The intersection between the trends of  $N_1$  and the shear stress  $\tau_{12}$  gives an estimate of the reciprocal of the fluid relaxation time.<sup>17</sup> In this case, we have  $\tau_r \approx 1/4 = 0.25\text{ s}$ . In Figure S2B, the linear viscoelastic response of PA1 is reported, showing that the trend of the elastic modulus  $G'$  is comparable yet lower and almost parallel to the one of the viscous modulus  $G''$  in the whole frequency range considered. The terminal slopes for the viscoelastic moduli, which should be approached in the range 0.1–1 rad/s (to be coherent with the steady test response), are not accessible in our operative conditions (mainly for the impossibility to increase the temperature by using the convection oven and simultaneously control the evaporation). Nevertheless, the experimental response of the sample is in agreement with the rheological fingerprint of a Boger fluid.<sup>17,40,41</sup>

Figure S3 gives the rheological properties of PA2. The viscosity shows a shear-thinning behavior with a zero-shear viscosity of roughly 3 Pa s (see Figure S3A). The viscoelastic response is typical of a non-well-entangled polymeric system, with a characteristic relaxation time of about 0.8 s and a plateau elastic modulus of about 1 Pa (Figure S3B).

Figure S4 shows the rheological characterization of WMS1. In panel A, a shear-thinning behavior with a zero-shear viscosity of about 10 Pa s is visible. The frequency sweep (Figure S4B) shows a Maxwell-like behavior with a single relaxation time of roughly 0.16 s and a well-defined plateau elastic modulus equal to 65 Pa. Both the steady and oscillatory measurements suggest that the micellar solution is characterized by long wormlike linear micelles.

Finally, Figure S5 displays the rheological properties of WMS2. From the point of view of the steady shear measurements (see Figure S5A), such a fluid behaves very similarly to WMS1, showing a shear thinning behavior with a zero-shear viscosity of roughly 10 Pa s. The frequency sweep (Figure S5B) yields a Maxwell-like behavior with a single relaxation time of about 10 s and a clearly visible plateau elastic modulus at 2 Pa. As above, both experiments suggest that the micellar solution is characterized by the presence of very long wormlike linear micelles.

The surface tension between the fluids and air has been measured through the pendant drop method.<sup>42</sup> The drop images have been acquired through a high-resolution charge-coupled device (CCD) camera (BV-7105H, Appro) equipped with a modular zoom lens system (Zoom 6000, Navitar). Light-emitting diodes provided a uniform bright background for optimal threshold and drop image

digitalization. The CCD camera was connected to a computer, and a commercial software (FTA32 Video 2.0, First Ten Angstroms) has been used to analyze the drop profile. For each fluid, 10 different tests have been performed at  $25^\circ\text{C}$ . The measured values of the surface tension are 0.045 N/m for PA1 (a pendant drop image is reported in Figure S7), 0.058 N/m for PA2, 0.031 N/m for WMS1, and 0.05 N/m for WMS2.

**Bubble Rupture Visualization.** A circular metallic ring with a radius  $R_b = 7.5\text{ mm}$  (for PA1), 9 mm (for PA2 and WMS1), or 4 mm (for WMS2) was pulled out from a liquid pool to produce a flat liquid film. The film thickness  $\delta$  at bubble rupture was calculated from the mass  $m$  of the initial amount of liquid deposited on the ring by solving the following equation:

$$\frac{m}{\rho} = \frac{4}{6}\pi(R_b + \delta)^3 - \frac{4}{6}\pi R_b^3 \quad (7)$$

where  $\rho$  is the fluid density and  $R_b$  is the radius of the ring, equal in our experiments to the radius attained by the bubble at rupture (for the four different fluids considered in this paper, we got  $\delta$  values between 10 and  $150\text{ }\mu\text{m}$ ). Cross-check of the film thickness was performed on WMS1 by means of the colors visible on the bubble, as the achieved film thickness was comparable to the visible light wavelength (see Figure 3B1). The ring was then placed above a sealed connection to a syringe pump (model 22, Harvard Apparatus) that insufflated air below the liquid film at a constant flow rate and room temperature. A self-centering lens mount aided the ring positioning (SCL60C, Thorlabs Inc.). A hot sharp needle with a tip radius of  $160\text{ }\mu\text{m}$  was placed above the bubble at a distance of  $R_b$  from the ring plane, aligned with the center of the ring. The rupture of the bubble was recorded by using a fast camera (i-speed 3, Olympus) at frame rates of 20 000–30 000 fps. The camera was tilted  $10^\circ$  from the horizontal to allow good visualization of the hole opening. Light-emitting diode lamps were used to avoid sample heating. A webcam was also employed for inflation observation (HD Pro Webcam C920, Logitech), as it can be watched online in Movies S2–S4, showing the puncturing and retraction of PA1 bubbles at IR = 20, 120, and  $250\text{ mm}^3/\text{s}$ . It is worth mentioning that we did not interrupt air pumping at bubble rupture. However, given the different time scales of the inflation ( $\sim\text{s}$ ) and rupture ( $\sim\text{ms}$ ) processes, this effect can be neglected.

The frames acquired by the high-speed camera and the webcam were processed through ImageJ Software (National Institutes of Health) to measure the arc  $a$  of the growing bubbles during inflation (see Figure S6) and the radius  $R$  of the opening hole during retraction, whose temporal trends are reported in Figure 3A2–C2 and 2B for the different fluids and inflation rates.

**Direct Numerical Simulations.** The mass balance, the momentum balance, and the constitutive equations on the liquid domain shown in Figure 1B1–B3 have been solved through the finite element method with an arbitrary Lagrangian Eulerian formulation. The numerical code uses stabilization techniques widely described in the literature, such as streamline upwind Petrov–Galerkin method and log conformation.<sup>43–45</sup> A detailed description of the algorithm employed to track the film surface is given in ref 46. As it can be seen in Figure 1B1–B3, the system has a symmetry axis coinciding with the  $z$  axis and a symmetry plane parallel to the  $r$  axis at  $z = 0$ ; thus, the physical domain could be reduced to a two-dimensional axisymmetric computational domain. The latter has been discretized by an unstructured mesh made of triangular elements. During the simulations, the hole broadens and the liquid film retracts toward the solid wall at  $r = L$ , making the mesh elements deform progressively. Every time the mesh quality went below a threshold, remeshing has been done and the computed velocity, pressure, and stress fields have been projected from the old mesh to the new one.<sup>47,48</sup> Preliminary convergence tests have been performed in space and time, that is, mesh resolution and time step for the numerical solution of the model equations have been selected such that invariance of the results upon further refinements has been ensured. Second-order time integration has been used. The details on the mathematical description of the system considered in the numerical simulations are given in the Supporting Information.<sup>49–51</sup>

## ■ ASSOCIATED CONTENT

### Supporting Information

The Supporting Information is available free of charge on the ACS Publications website at DOI: [10.1021/acs.langmuir.8b00520](https://doi.org/10.1021/acs.langmuir.8b00520).

Outline of the problem for direct numerical simulations; snapshots of the punctured bubble after slow and fast inflation; shear viscosity, first normal stress difference, and shear stress of 0.05 wt % solution of PA1; shear viscosity of PA2, WMS1, and WMS2; PA1, PA2, WMS1, and WMS2 linear elastic modulus  $G'$  and viscous modulus  $G''$ ; sketch of the time evolution of the arc; deformation history of the PA1 film; microscopic image of a pendant PA1 drop in air; sketch of the experimental system at the beginning and at the end of bubble inflation; sketch of the numerical system at the beginning and at the end of film stretching; PA1 rheological and geometrical parameters; and geometrical and rheological parameters for the finite element numerical simulations (PDF)

Rupture of bubble gum at two different inflation rates (AVI)

Hole opening of the PA1 film at IR = 20 m<sup>3</sup>/s (AVI)

Hole opening of the PA1 film at IR = 120 m<sup>3</sup>/s (AVI)

Hole opening of the PA1 film at IR = 250 m<sup>3</sup>/s (AVI)

## ■ AUTHOR INFORMATION

### Corresponding Authors

\*E-mail: [massimiliano.villone@unina.it](mailto:massimiliano.villone@unina.it). Phone: +390817682280 (M.M.V.).

\*E-mail: [edimaino@unina.it](mailto:edimaino@unina.it). Phone: +390817682511 (E.D.M.).

### ORCID

Ernesto Di Maio: [0000-0002-3276-174X](https://orcid.org/0000-0002-3276-174X)

### Author Contributions

D.T. and R.P. equally contributed to this work. M.M.V., G.D., E.D.M., N.G., and P.L.M. designed the research; D.T., V.F., R.P., E.D.M., and A.L. performed the experiments; M.M.V. and G.D. performed the numerical simulations; all authors analyzed the data; D.T., R.P., M.M.V., G.D., E.D.M., N.G., and P.L.M. wrote the paper.

### Notes

The authors declare no competing financial interest.

## ■ ACKNOWLEDGMENTS

The authors wish to thank Massimiliano Fraldi of the Department of Structures for Engineering and Architecture at The University of Naples Federico II and Martien A. Hulsen of the Department of Mechanical Engineering at the Eindhoven University of Technology for fruitful discussion. Elasticity in Bubble Breaking (ELTYBUNG) Project funded by the University of Naples Federico II (DR/2017/409) is acknowledged for partial support of this work.

## ■ REFERENCES

- (1) Duprè, M. A. Sixième memoire sur la theorie mécanique de la chaleur. *Ann. Chim. Phys.* **1867**, *11*, 194–220.
- (2) Taylor, G. The dynamics of thin sheets of fluid. III. Disintegration of fluid sheets. *Proc. R. Soc. London, Ser. A* **1959**, *253*, 313–321.
- (3) Culick, F. E. C. Comments on a ruptured soap film. *J. Appl. Phys.* **1960**, *31*, 1128–1129.
- (4) Debrégeas, G.; de Gennes, P.-G.; Brochard-Wyart, F. The life and death of bare viscous bubbles. *Science* **1998**, *279*, 1704–1707.

- (5) Clasen, C.; Phillips, P. M.; Palangetic, L.; Vermant, J. Dispensing of Rheologically Complex Fluids: The Map of Misery. *AIChE J.* **2012**, *58*, 3242–3255.

- (6) Morrison, N. F.; Harlen, O. G. Viscoelasticity in inkjet printing. *Rheol. Acta* **2010**, *49*, 619–632.

- (7) Cooper-White, J. J.; Fagan, J. E.; Tirtaatmadja, V.; Lester, D. R.; Boger, D. V. Drop formation dynamics of constant low-viscosity, elastic fluids. *J. Non-Newtonian Fluid Mech.* **2002**, *106*, 29–59.

- (8) Davidson, M. R.; Harvie, D. J. E.; Cooper-White, J. J. Simulations of pendant drop formation of a viscoelastic liquid. *Korea Aust. Rheol. J.* **2006**, *18*, 41–49.

- (9) Tirtaatmadja, V.; McKinley, G. H.; Cooper-White, J. J. Drop formation and breakup of low viscosity elastic fluids: Effects of molecular weight and concentration. *Phys. Fluids* **2006**, *18*, 043101.

- (10) Evers, L. J.; Shulepov, S. Y.; Frens, G. Bursting Dynamics of Thin Free Liquid Films from Newtonian and Viscoelastic Solutions. *Phys. Rev. Lett.* **1997**, *79*, 4850–4853.

- (11) Sabadini, E.; Ungarato, R. F. S.; Miranda, P. B. The elasticity of soap bubbles containing worm like micelles. *Langmuir* **2014**, *30*, 727–732.

- (12) Bloksma, A. H. A calculation of the shape of the alveograms of some rheological model substances. *Cereal Chem.* **1957**, *34*, 126–136.

- (13) Dobraszczyk, B. J. Development of a new dough inflation system to evaluate doughs. *J. Am. Assoc. Cereal Chem.* **1997**, *42*, 516–519.

- (14) Dobraszczyk, B. J.; Roberts, C. A. Strain hardening and dough gas cell-wall failure in biaxial extension. *J. Cereal Sci.* **1994**, *20*, 265–274.

- (15) Charalambides, M.; Wanigasooriya, L.; Williams, G.; Chakrabarti, S. Biaxial deformation of dough using the bubble inflation technique. I. Experimental. *Rheol. Acta* **2002**, *41*, 532–540.

- (16) Charalambides, M.; Wanigasooriya, L.; Williams, G. Biaxial deformation of dough using the bubble inflation technique. II. Numerical modelling. *Rheol. Acta* **2002**, *41*, 541–548.

- (17) Boger, D. V. A highly elastic constant-viscosity fluid. *J. Non-Newtonian Fluid Mech.* **1977**, *3*, 87–91.

- (18) Lhuissier, H.; Villermaux, E. Soap films burst like flapping flags. *Phys. Rev. Lett.* **2009**, *103*, 054501.

- (19) Savva, N.; Bush, J. W. M. Viscous sheet retraction. *J. Fluid Mech.* **2009**, *626*, 211–240.

- (20) Čopar, S.; Kodre, A. One-dimensional simulation of thin liquid-film-edge retraction. *Phys. Rev. E: Stat., Nonlinear, Soft Matter Phys.* **2010**, *82*, 056307.

- (21) Trittel, T.; John, T.; Tsuji, K.; Stannarius, R. Rim instability of bursting thin smectic films. *Phys. Fluids* **2013**, *25*, 052106.

- (22) Villone, M. M.; D'Avino, G.; Di Maio, E.; Hulsen, M. A.; Maffettone, P. L. Modeling and simulation of viscoelastic film retraction. *J. Non-Newtonian Fluid Mech.* **2017**, *249*, 26–35.

- (23) Larson, R. G. *Constitutive Equations for Polymer Solutions and Melts*; Butterworths: Stoneham, 1988.

- (24) Bird, R.; Byron, R.; Armstrong, C.; Hassager, O. Dynamics of Polymeric Liquids. *Fluid Mechanics*; John Wiley and Sons Inc.: New York, 1987; Vol. 1.

- (25) Macosko, C. W. *Rheology Principles, Measurements, and Applications*; VCH Publishers Inc.: New York, 1994; p 111.

- (26) Bird, J. C.; de Ruiter, R.; Courbin, L.; Stone, H. A. Daughter bubble cascades produced by folding of ruptured thin films. *Nature* **2010**, *465*, 759–762.

- (27) McKinley, G. H. Dimensionless groups for understanding free surface flows of complex fluids. *Soc. Rheol. Bull.* **2005**, *6*, 9–20.

- (28) Chatraei, S.; Macosko, C. W.; Winter, H. H. Lubricated squeezing flow: a new biaxial extensional rheometer. *J. Rheol.* **1981**, *25*, 433–443.

- (29) Stein, D. J.; Spera, F. J. Rheology and microstructure of magmatic emulsions: theory and experiments. *J. Volcanol. Geotherm. Res.* **1992**, *49*, 157–174.

- (30) Banhart, J.; Stanzick, H.; Helfen, L.; Baumbach, T. Metal foam evolution studied by synchrotron radiography. *Appl. Phys. Lett.* **2001**, *78*, 1152–1154.

(31) Tamaro, D.; D'Avino, G.; Di Maio, E.; Pasquino, R.; Villone, M. M.; Gonzales, D.; Groombridge, M.; Grizzuti, N.; Maffettone, P. L. Validated modeling of bubble growth, impingement and retraction to predict cell-opening in thermoplastic foaming. *Chem. Eng. J.* **2016**, *28*, 492–502.

(32) Taki, K.; Tabata, K.; Kihara, S.-i.; Ohshima, M. Bubble coalescence in foaming process of polymers. *Polym. Eng. Sci.* **2006**, *46*, 680–690.

(33) Eames, I.; Peng, T.; Khaw, M.; Bouremel, Y. How to make the perfect pancake. *Math. Today* **2016**, *2*, 125–132.

(34) Cho, Y. S.; Laskowski, J. S. Bubble coalescence and its effect on dynamic foam stability. *Can. J. Chem. Eng.* **2002**, *80*, 299–305.

(35) Parmigiani, A.; Faroughi, S.; Huber, C.; Bachmann, O.; Su, Y. Bubble accumulation and its role in the evolution of magma reservoirs in the upper crust. *Nature* **2016**, *532*, 492–495.

(36) Mader, H. M.; Zhang, Y.; Phillips, J. C.; Sparks, R. S. J.; Sturtevant, B.; Stolper, E. Experimental simulations of explosive degassing of magma. *Nature* **1994**, *372*, 85–88.

(37) Isenberg, C. *The Science of Soap Films and Soap Bubbles*; Dover Publisher: New York, 1992.

(38) Gaudino, D.; Pasquino, R.; Grizzuti, N. Adding salt to a surfactant solution: Linear rheological response of the resulting morphologies. *J. Rheol.* **2015**, *59*, 1363–1375.

(39) Gaudino, D.; Pasquino, R.; Stellbrink, J.; Szekeley, N.; Krutyeva, M.; Radulescu, A.; Pyckhout-Hintzen, W.; Grizzuti, N. The role of the binding salt sodium salicylate in semidilute ionic cetylpyridinium chloride micellar solutions: a rheological and scattering study. *Phys. Chem. Chem. Phys.* **2017**, *19*, 782–790.

(40) Calado, V. M. A.; White, J. M.; Muller, S. J. Transient behavior of Boger fluids under extended shear flow in a cone-and-plate rheometer. *Rheol. Acta* **2005**, *44*, 250–261.

(41) Snijkers, F.; D'Avino, G.; Maffettone, P. L.; Greco, F.; Hulsen, M. A.; Vermant, J. Effect of viscoelasticity on the rotation of a sphere in shear flow. *J. Non-Newtonian Fluid Mech.* **2011**, *166*, 363–372.

(42) del Rio, O. L.; Neumann, A. W. Axisymmetric drop shape analysis: computational methods for the measurement of interfacial properties from the shape and dimensions of pendant and sessile drops. *J. Colloid Interface Sci.* **1997**, *196*, 136–147.

(43) Guénette, R.; Fortin, M. A new mixed finite element method for computing viscoelastic flows. *J. Non-Newtonian Fluid Mech.* **1995**, *60*, 27–52.

(44) Bogaerds, A. C. B.; Grillet, A. M.; Peters, G. W. M.; Baaijens, F. P. T. Stability analysis of polymer shear flows using the extended pom–pom constitutive equations. *J. Non-Newtonian Fluid Mech.* **2002**, *108*, 187–208.

(45) Brooks, A. N.; Hughes, T. J. R. Streamline upwind/Petrov–Galerkin formulations for convection dominated flows with particular emphasis on the incompressible Navier–Stokes equations. *Comput. Meth. Appl. Mech. Eng.* **1982**, *32*, 199–259.

(46) Villone, M. M.; Hulsen, M. A.; Anderson, P. D.; Maffettone, P. L. Simulations of deformable systems in fluids under shear flow using an arbitrary Lagrangian Eulerian technique. *Comput. Fluids* **2014**, *90*, 88–100.

(47) Hu, H. H.; Patankar, N. A.; Zhu, M. Y. Direct numerical simulations of fluid–solid systems using the arbitrary Lagrangian–Eulerian technique. *J. Comput. Phys.* **2001**, *169*, 427–462.

(48) Jaensson, N. O.; Hulsen, M. A.; Anderson, P. D. Stokes–Cahn–Hilliard formulations and simulations of two-phase flows with suspended rigid particles. *Comput. Fluids* **2015**, *111*, 1–17.

(49) Quinzani, L. M.; McKinley, G. H.; Brown, R. A.; Armstrong, R. C. Modeling the rheology of polyisobutylene solutions. *J. Rheol.* **1990**, *34*, 705–748.

(50) Song, M.; Tryggvason, G. The formation of thick borders on an initially stationary fluid sheet. *Phys. Fluids* **1999**, *11*, 2487–2493.

(51) McKinley, G. H.; Byars, J. A.; Brown, R. A.; Armstrong, R. C. Observations on the elastic instability in cone-and-plate and parallel-plate flows of a polyisobutylene Boger fluid. *J. Non-Newtonian Fluid Mech.* **1991**, *40*, 201–229.